Physica D 434 (2022) 133226

Contents lists available at ScienceDirect

Physica D

journal homepage: www.elsevier.com/locate/physd

Self-similar collapse of three vortices in the generalised Euler and quasi-geostrophic equations

Jean N. Reinaud *, David G. Dritschel, Richard K. Scott

Mathematical Institute, University of St Andrews, St Andrews, KY169 SS, UK

ARTICLE INFO

Article history:
Received 9 September 2021
Received in revised form 28 February 2022
Accepted 1 March 2022
Available online 16 March 2022
Communicated by Stephen Wiggins

Keywords:
Vortex dynamics
Point vortices
Vortex collapse
Generalised Euler equations

ABSTRACT

We revisit the classical problem of the self-similar, finite-time collapse of three vortices. We extend the study to the generalised two-dimensional Euler equations as well as the generalised three-dimensional quasi-geostrophic equations. In both these situations, the flow is fully controlled by a materially-conserved field of a generalised vorticity (or potential vorticity) related to the streamfunction by a modified Poisson's equation, in which the standard Laplacian is replaced by a fractional Laplacian. We first determine the conditions for the self-similar collapse of three *point* vortices, as well as the *collapse time* in a broad parameter space. We then consider the evolution of *finite-core*, two-dimensional and three-dimensional vortices under initial conditions corresponding to the collapse of equivalent point vortices. We show that the interaction precipitates the merger of the two like-signed vortices in the vortex triad.

1. Introduction

Vortices, or swirling masses of fluid, are ubiquitous in the fluid dynamics of both two-dimensional (2D) and three-dimensional (3D) flows, and their interactions play a central role in many fundamental processes. For example, they collectively drive the dynamics of 2D incompressible turbulence, see e.g. [1], where the distribution of vortex sizes has been shown to play a fundamental role in the evolution of energy across scales in both the freely-decaying and forced cases [2,3]. In the oceans, vortices contribute a large part of the mass transport, see [4], while in Jupiter's atmosphere, stable arrays of vortices have recently been observed in polar latitudes [5].

The merger of two like-signed vortices is associated with the inverse energy cascade in 2D turbulence through the generation of larger vortices, while also contributing to the direct enstrophy cascade through the generation of small-scale debris and filaments. Vortex merger also plays a fundamental role in the mixing of heat and chemical constituents in oceanic and atmospheric flows.

In this paper we consider a type of interaction between three vortices that leads to their collapse toward a single point in finite time. The collapse of three vortices is a special case of the general collapse of N vortices, albeit arguably the most likely case statistically. For point vortices, this collapse takes the form of an exact self-similar reduction of the vortex separations to zero. For equivalent finite-core vortices, the collapse does not remain exactly self-similar but precipitates a strong interaction between the vortices, and in particular the merger of the two like-signed vortices of the vortex triad. While the natural setting in which to study these interactions is in the context of 2D flow, the same ideas can be applied to 3D quasi-geostrophic flows. These introduce a vertical structure to the vorticity distribution while retaining a layerwise 2D flow, and can therefore be regarded as lying somewhere between the 2D and fully 3D systems.

The mathematical formalism to study flows with vorticity was first introduced by Helmholtz [6]. Kirchhoff [7] introduced and used the notion of point vortices in a 2D flow. Poincaré [8] proved that a system of three 2D point vortices was integrable. Gröbli [9] studied for the first time the self-similar motion of three point vortices. Later Synge [10] provided a classification of their motion. The motion of three point vortices was also independently studied by Novikov [11], Aref [12], Tavantzis and Ting [13]. The problem of the self-similar collapse for 2D vortices has been extensively studied in the literature, e.g. by Novikov and Sedov [14], Kimura [15,16,17], Aref [18], and more recently by Krishnamurthy and Stremler [19]. The collapse interaction of finite-area 2D vortices has been studied by Vosbeek et al. [20]. Badin and Barry [21] extended the study of the collapse of three point vortices to the 2D generalised Euler equations, including the so-called 'surface quasi-geostrophic' (SQG) equations. The SQG equations are relevant to the surface potential temperature dynamics in rotating stratified environments such as

* Corresponding author.
E-mail addresses: jean.reinaud@st-andrews.ac.uk (J.N. Reinaud), david.dritschel@st-andrews.ac.uk (D.G. Dritschel), richard.scott@st-andrews.ac.uk (R.K. Scott).

https://doi.org/10.1016/j.physd.2022.133226

Table 1
Summary of the classical models.

n	α	β	Name	Green's function
2	1	0	2D EulerSQG	$(2\pi)^{-1}\log r - (2\pi r)^{-1}$
	1/2	1		
3	1	1	3D QGNone	$-(4\pi r)^{-1}(2\pi^2)^{-1}\log r$
	3/2	0		

planetary atmospheres and oceans. The general motion of three SQG point vortices has been studied by [22] while the motion of three ageostrophic point vortices is addressed in [23]. More recently, Reinaud [24] revisited the collapse of point vortices and the collapse interaction of finite-core vortices in both the 3D quasi-geostrophic (QG) and the SQG equations. The present contribution is the natural extension to the latter study beyond the classical 2D Euler, SQG and 3D QG systems.

The 2D Euler and SQG equations are only two members of a family of 2D dynamical models depending on a single parameter, α, defined fully in the following section. Here, we refer to this family as the generalised Euler equations. The important dynamical feature is that the locality of vortex interactions decreases as the parameter α increases [25]. Similarly, the 3D QG system can be viewed as a single member of a family of 3D models with layerwise-2D flow fields. A remarkable feature of the subsequent analysis for point vortices is that the three-vortex evolution in both the 2D and 3D generalised systems is identical and dependent only on a single parameter β.

The paper is organised as follows. Section 2 describes the governing equations of the system. The conditions leading to the self-similar collapse of a triad of point vortices are derived in Section 3. Results for the collapse of point vortices are presented in Section 4, while the results for the collapse interaction of three 2D finite-area vortices and three 3D finite-volume vortices are presented in Sections 5 and 6 respectively. Concluding remarks are given in Section 7.

2. Mathematical model

We consider the following dynamical system in $\mathbb{R}^n$,

$$-(-\nabla^2)^\alpha \varphi = q, \tag{1}$$

$$\frac{\partial q}{\partial t} + u\frac{\partial q}{\partial x} + v\frac{\partial q}{\partial y} = 0. \tag{2}$$

$$u = -\frac{\partial \varphi}{\partial y}, \quad \& \quad v = \frac{\partial \varphi}{\partial x}, \tag{3}$$

where φ is the streamfunction, q is the active scalar, x, y are the first two coordinates of $\mathbb{R}^n$ and u, v are the first two components of the velocity field. ∇^2 is n-dimensional Laplacian and $0 < \alpha < n/2$. The special though important limiting case $\alpha = n/2$ will also be discussed. Although the results presented in the paper are valid for all $n \geq 2$, we are primarily concerned with the cases $n = 2$ and $n = 3$, relevant to physical systems such as fluids. For $n = 2$, the equations are known as the generalised 2D Euler equations, with the special case $\alpha = n/2 = 1$ corresponding to the standard Euler equations governing the evolution of a 2D incompressible flow. Another important case is the surface quasi-geostrophic (SQG) model, discussed in [26], corresponding to $n = 2$ and $\alpha = 1/2$. For $n = 3$, the equations are the generalised 3D Quasi-Geostrophic (QG) equations. For reference, the standard 3D QG equations correspond to $n = 3$ and $\alpha = 1$. The parameters for the three main standard physical models are summarised in Table 1.

For $n = 2$, the flow is planar and 2D in the $(x, y)-$plane. Even for $n > 2$, Eq. (2) implies that advection remains 2D, i.e. restricted to the $(x, y)-$plane.

Eq. (1) can be formally inverted using the appropriate Green's function

$$G(\boldsymbol{x}; \boldsymbol{x}') = -\frac{C_{n,-\alpha}}{|\boldsymbol{x} - \boldsymbol{x}'|^\beta}, \tag{4}$$

given e.g. by Stinga [27] in an unbounded domain with

$$\beta = n - 2\alpha, \quad \text{for } \beta \neq 0, \tag{5}$$

and

$$C_{n,-\alpha} = \frac{\Gamma(n/2 - \alpha)}{4^\alpha \Gamma(\alpha)\pi^{n/2}}, \tag{6}$$

where Γ is the standard Gamma function, $\Gamma(x) = \int_0^\infty u^{x-1}e^{-u}\,du$ for $x \in (0, \infty)$.

As mentioned above, the standard 2D Euler equations correspond to $\alpha = n/2 = 1$, hence $\beta = 0$. In this case, the Green's function $G(\boldsymbol{x}; \boldsymbol{x}') = (2\pi)^{-1}\log|\boldsymbol{x} - \boldsymbol{x}'|$. A similar Green's function is obtained for $n = 3$ and $\alpha = 1.5$, namely $G(\boldsymbol{x}; \boldsymbol{x}') = (2\pi^2)^{-1}\log|\boldsymbol{x} - \boldsymbol{x}'|$. The general formulae to recover these Green's functions are given in [27]. We will see that the relations derived in the next section to determine the conditions for collapse with $\beta \neq 0$ are in fact also valid for the case $\beta = 0$.

3. Conditions for self-similar collapse

We consider 3 active particles of strength κ_i' located at $\boldsymbol{x}_i$ in an unbounded domain. As these particles induce a circulating flow around them, we will henceforth call these active particles 'point vortices' for all α for simplicity. The strength κ_i' of vortex i is the space-integrated active scalar multiplied by $C_{n,-\alpha}$. The active scalar field is therefore

$$q(\boldsymbol{x}) = \frac{1}{C_{n,-\alpha}} \sum_{i=1}^{3} \kappa_i' \,\delta(\boldsymbol{x} - \boldsymbol{x}_i), \tag{7}$$

where $\delta()$ is the Dirac distribution in $\mathbb{R}^n$. The streamfunction induced by the three vortices then follows from the definition of Green's function:

$$\varphi(\boldsymbol{x}) = -\sum_{i=1}^{3} \frac{\kappa_i'}{|\boldsymbol{x} - \boldsymbol{x}_i|^\beta}, \quad \forall \boldsymbol{x} \neq \boldsymbol{x}_i. \tag{8}$$

Following [24] we denote $\boldsymbol{\ell}_{ij} = \boldsymbol{x}_i - \boldsymbol{x}_j$. Since the vortices move only horizontally, parallel to the (x, y)-plane, vortex collapse to a single point can occur iff all three vortices are initially in the same (x, y)-plane. The two non-zero velocity components of point vortex i are given by

$$(u_i, v_i) = \sum_{j=1, j\neq i}^{3} \frac{\kappa_j}{|\boldsymbol{\ell}_{ij}|^{\beta+2}}(-\ell_{ij}^y, \ell_{ij}^x), \tag{9}$$

where $\kappa_i = \beta\kappa_i'$, and ℓ_{ij}^x and ℓ_{ij}^y are the x and y-components of $\boldsymbol{\ell}_{ij}$. Eq. (9) and the formulae derived from it are formally valid even for $\beta = 0$, i.e. for $\alpha = n/2$. Furthermore, this dynamical system is Hamiltonian, and may be written

$$u_i = \frac{\mathrm{d}x_i}{\mathrm{d}t} = -\frac{1}{\kappa_i}\frac{\partial H}{\partial y_i}, \quad v_i = \frac{\mathrm{d}y_i}{\mathrm{d}t} = \frac{1}{\kappa_i}\frac{\partial H}{\partial x_i}, \tag{10}$$

where

$$H = -\frac{1}{2}\sum_{i=1}^{3}\sum_{j=1, j\neq i}^{3} \frac{\kappa_i\kappa_j}{|\boldsymbol{\ell}_{ij}|^\beta}. \tag{11}$$

is the 'excess energy'.

The equations governing the evolution of the squared distances between the vortices $s_1^2 = |\boldsymbol{\ell}_{23}|^2$, $s_2^2 = |\boldsymbol{\ell}_{13}|^2$ and $s_3 = |\boldsymbol{\ell}_{12}|$

follow from (9) and read

$$\frac{\mathrm{d}s_1^2}{\mathrm{d}t} = 2\kappa_1\Delta\left(\frac{1}{s_2^{\beta+2}} - \frac{1}{s_3^{\beta+2}}\right), \tag{12}$$

$$\frac{\mathrm{d}s_2^2}{\mathrm{d}t} = 2\kappa_2\Delta\left(\frac{1}{s_3^{\beta+2}} - \frac{1}{s_1^{\beta+2}}\right), \tag{13}$$

$$\frac{\mathrm{d}s_3^2}{\mathrm{d}t} = 2\kappa_3\Delta\left(\frac{1}{s_1^{\beta+2}} - \frac{1}{s_2^{\beta+2}}\right), \tag{14}$$

where $\Delta = \ell_{12}^x\ell_{23}^y - \ell_{12}^y\ell_{23}^x$ is twice the area of the triangle formed by the three vortices, assuming the vortices $1 \to 2 \to 3$ are organised in a counter-clockwise direction. We assume that the collapse evolution of the distances s_i is self-similar, i.e. $s_i(t) = f(t)\mathfrak{s}_i$, where $\mathfrak{s}_i \equiv s_i(0)$. Heron's formula for the squared area of a triangle, $4\Delta^2 = 2(s_1^2s_2^2 + s_1^2s_3^2 + s_2^2s_3^2) - s_1^4 - s_2^4 - s_3^4$, implies that $\Delta(t) = f^2(t)\,\mathfrak{d}$, where $\mathfrak{d} \equiv \Delta(0)$. Substituting in (12), we find

$$\frac{\mathrm{d}s_1^2}{\mathrm{d}t} = \mathfrak{s}_1^2\frac{\mathrm{d}f^2}{\mathrm{d}t} = 2\kappa_1\mathfrak{d}\frac{1}{f^\beta(t)}\left(\frac{1}{\mathfrak{s}_2^{\beta+2}} - \frac{1}{\mathfrak{s}_3^{\beta+2}}\right). \tag{15}$$

Solving Eq. (15) gives

$$f(t) = \left(1 - \frac{t}{\tau}\right)^{\frac{1}{\beta+2}}, \tag{16}$$

where $f(t)$ reduces to 0 at the finite *collapse time*

$$\tau = -\frac{\mathfrak{s}_1^2}{(\beta+2)\kappa_1\mathfrak{d}\left(\frac{1}{\mathfrak{s}_2^{\beta+2}} - \frac{1}{\mathfrak{s}_3^{\beta+2}}\right)}. \tag{17}$$

The uniqueness of τ implies Eqs. (13) and (14) must also lead to the same value. This results in the following two constraints

$$\kappa_1\mathfrak{s}_1^\beta(\mathfrak{s}_3^{\beta+2} - \mathfrak{s}_2^{\beta+2}) = \kappa_2\mathfrak{s}_2^\beta(\mathfrak{s}_1^{\beta+2} - \mathfrak{s}_3^{\beta+2}) = \kappa_3\mathfrak{s}_3^\beta(\mathfrak{s}_2^{\beta+2} - \mathfrak{s}_1^{\beta+2}). \tag{18}$$

A further constraint comes from the fact that the scaled Hamiltonian

$$H' = -2H = \frac{\kappa_1\kappa_2}{s_3^\beta} + \frac{\kappa_1\kappa_3}{s_2^\beta} + \frac{\kappa_2\kappa_3}{s_1^\beta} \tag{19}$$

is invariant by construction. This invariance implies

$$\frac{\kappa_1\kappa_2}{s_3^\beta(t)} + \frac{\kappa_1\kappa_3}{s_2^\beta(t)} + \frac{\kappa_2\kappa_3}{s_1^\beta(t)} = \frac{1}{f^\beta(t)}\left(\frac{\kappa_1\kappa_2}{\mathfrak{s}_3^\beta} + \frac{\kappa_1\kappa_3}{\mathfrak{s}_2^\beta} + \frac{\kappa_2\kappa_3}{\mathfrak{s}_1^\beta}\right),$$

leading to

$$\frac{\kappa_1\kappa_2}{\mathfrak{s}_3^\beta} + \frac{\kappa_1\kappa_3}{\mathfrak{s}_2^\beta} + \frac{\kappa_2\kappa_3}{\mathfrak{s}_1^\beta} = 0, \tag{20}$$

or the trivial solution $f(t) = 1$ which corresponds to a relative equilibrium. Note that for $\alpha = n/2$, corresponding to $\beta = 0$, the scaled Hamiltonian H' has the form

$$\begin{aligned}&\kappa_1\kappa_2\log s_3(t) + \kappa_1\kappa_3\log s_2(t) + \kappa_2\kappa_3\log s_1(t)\\ &= (\kappa_1\kappa_2 + \kappa_1\kappa_3 + \kappa_2\kappa_3)\log f(t) +\\ &\quad \kappa_1\kappa_2\log\mathfrak{s}_3 + \kappa_1\kappa_3\log\mathfrak{s}_2 + \kappa_2\kappa_3\log\mathfrak{s}_1\end{aligned} \tag{21}$$

which is invariant iff

$$\kappa_1\kappa_2 + \kappa_1\kappa_3 + \kappa_2\kappa_3 = 0.$$

This condition is formally equivalent to Eq. (20) with $\beta = 0$. Hence Eq. (20) is also valid in this special case.

One might expect additional constraints to arise from conservation of linear and angular impulse. Their conservation arises from the fact that the Green's function $G(\boldsymbol{x};\boldsymbol{x}')$ depends only on the difference $\boldsymbol{x} - \boldsymbol{x}'$. This implies

$$\frac{\partial G}{\partial x} = -\frac{\partial G}{\partial x'}, \quad \& \quad \frac{\partial G}{\partial y} = -\frac{\partial G}{\partial y'}. \tag{22}$$

This anti-symmetry, also present in the special case $\beta = 0$, implies conservation of the linear impulse, $\boldsymbol{I} = \kappa_1\boldsymbol{x}_1 + \kappa_2\boldsymbol{x}_2 + \kappa_3\boldsymbol{x}_3$. Since only the x and y-components of the position $\boldsymbol{x}_i$ of vortex i are time-dependent, the only two non-trivial constraints are given by I_x and I_y, the x and y-components of $\boldsymbol{I}$ respectively. The anti-symmetry of G also implies conservation of the angular impulse, $J = \kappa_1(x_1^2+y_1^2) + \kappa_2(x_2^2+y_2^2) + \kappa_3(x_3^2+y_3^2)$. These quantities however are not functions only of the distances s_1, s_2 and s_3. Nonetheless, following [18], we can combine I_x, I_y and J to form an invariant quantity $L = (\kappa_1+\kappa_2+\kappa_3)J - I_x^2 - I_y^2$ depending only on these distances. For self-similar collapse, L takes the form

$$L = f^2(t)\left(\kappa_1\kappa_2\mathfrak{s}_3^2 + \kappa_1\kappa_3\mathfrak{s}_2^2 + \kappa_2\kappa_3\mathfrak{s}_1^2\right),$$

which is invariant iff

$$\kappa_1\kappa_2\mathfrak{s}_3^2 + \kappa_1\kappa_3\mathfrak{s}_2^2 + \kappa_2\kappa_3\mathfrak{s}_1^2 = 0, \tag{23}$$

or again if the point vortices are in relative equilibrium, $f(t) = 1$.

We have thus determined three scalar constraints, Eqs. (18), (20) and (23), on the rescaled vortex strengths κ_i and the distances $\mathfrak{s}_i$ separating them. The constraints, however, are not independent: one can show that (20) and (23) imply (18).

Without loss of generality, we take $\kappa_1 = 1$ and $\mathfrak{s}_3 = 1$, which sets a time and a length scale for the problem. We then choose values for β, κ_2 and $\mathfrak{s}_1$, and use these to solve Eqs. (20) and (23) to find $\mathfrak{s}_2$ and κ_3. Eq. (23) gives

$$\kappa_3 = -\frac{\kappa_2}{\mathfrak{s}_2^2 + \kappa_2\mathfrak{s}_1^2}. \tag{24}$$

Note that this implies that κ_3 and κ_2 have opposite signs. The fact that not all vortices can have the same sign is a requirement for vortex collapse, see e.g. [14]. Basically, the angular impulse $J = \kappa_1(x_1^2+y_1^2) + \kappa_2(x_2^2+y_2^2) + \kappa_3(x_3^2+y_3^2)$ must be zero, and this can only be achieved if the strengths have opposite signs.

Substituting κ_3 into (20) leads to an equation to determine $\mathfrak{s}_2$,

$$\mathfrak{s}_2^{\beta+2} + \kappa_2\frac{\mathfrak{s}_1^{\beta+2} - 1}{\mathfrak{s}_1^\beta}\mathfrak{s}_2^\beta - 1 = 0, \tag{25}$$

which is solved numerically by dichotomy until the value of $\mathfrak{s}_2$ changes by less than 10^{-12}. (Newton–Raphson does not always converge.) Not all solutions to these equations correspond to a physical vortex triad. The physically relevant solutions are those for which x_3 and y_3 are real numbers. Geometrically, this means that the circle centred at $\boldsymbol{x}_1$ and of radius $\mathfrak{s}_2$, and the circle centred at $\boldsymbol{x}_2$ and of radius $\mathfrak{s}_1$ intersect at $\boldsymbol{x}_3$, by definition. If the two circles do not intersect, collapse is not possible. Without loss of generality, we take $\boldsymbol{x}_1(0) = (-0.5, 0, 0)$ and $\boldsymbol{x}_2(0) = (0.5, 0, 0)$. Then the initial location of the third vortex is determined from the distances $\mathfrak{s}_1$ and $\mathfrak{s}_2$

$$x_3(0) = \frac{\mathfrak{s}_2^2 - \mathfrak{s}_1^2}{2}. \tag{26}$$

Then $y_3 > 0$ (counter-clockwise orientation) is given by

$$y_3(0) = \sqrt{\mathfrak{s}_1^2 - (0.5 - x_3(0))^2}, \tag{27}$$

which is real-valued provided $\mathfrak{s}_1^2 - (0.5 - x_3(0))^2 \geq 0$. Without loss of generality, we can set $0 < \kappa_2 \leq \kappa_1$ so that the second vortex is the weaker of the two positive vortices. Then, Eq. (24) implies $\kappa_3 < 0$. For vortex collapse, $ds_i^2/dt < 0$, $i = 1, 2, 3$, imply $\mathfrak{s}_1 < \mathfrak{s}_3 < \mathfrak{s}_2$. In particular $\mathfrak{s}_1 < 1$.

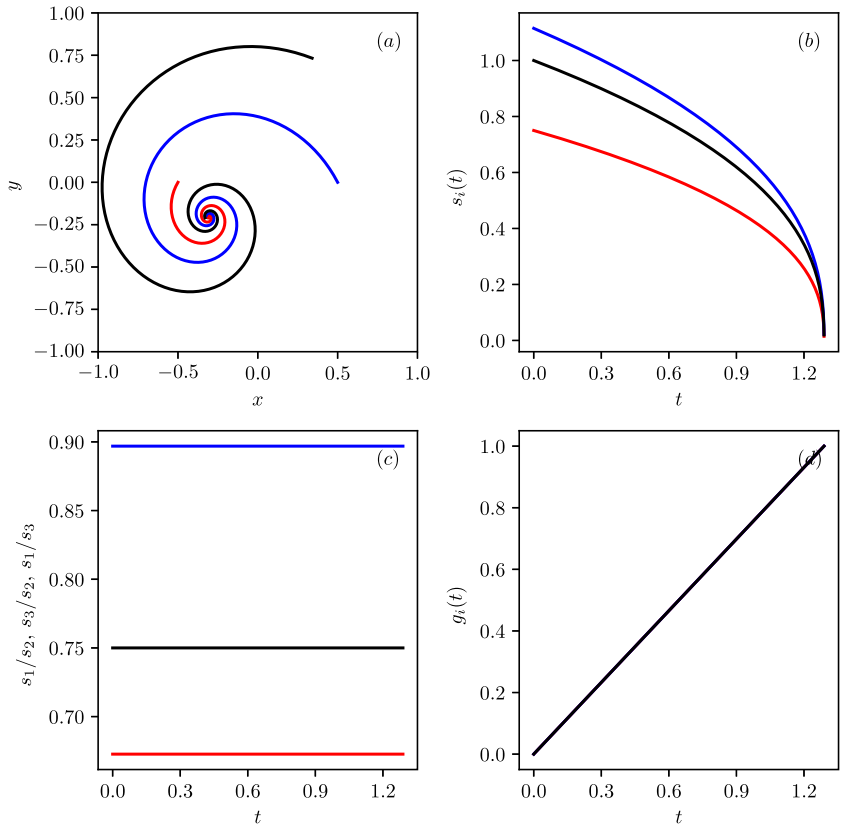

Fig. 1. Evolution of the three point vortices for $\beta = 0.5$, $\kappa = 0.5$ and $s = 0.75$ over the interval $0 \le t \le 1.289$: (a) trajectories of the point vortices, with vortex 1 in red, vortex 2 in blue and vortex 3 in black, (b) distances $s_i(t)$ between the vortices, (c) distance ratios, (d) geometrical functions $g_i(t)$. For panels (b) & (d), $i = 1$ is in red, $i = 2$ is in blue and $i = 3$ is in black. In panel (c), s_1/s_2 is in red, s_3/s_2 is in blue and s_1/s_3 is in black.

Table 2
Parameters for the finite-time collapse of three point vortices with $\kappa_2 = 0.5$ and $\mathfrak{s}_1 = 0.75$.

Case	β	κ_3	$\mathfrak{s}_2$	τ
I	0.5	−0.32799934672702413	1.1149633536646144	1.2890703487205131
II	1.5	−0.31486239284668249	1.1431296077175070	0.58167602508973415

4. Results for point vortices

We next present a selection of results for the finite-time collapse of three point vortices. The conditions for collapse depend on three parameters, β, κ_2 and $\mathfrak{s}_1$, offering a very large parameter space. Recall that $0 < \mathfrak{s}_1 \le 1$ and $0 < \beta < n$.

We first focus on two specific cases. We set $\kappa_2/\kappa_1 = 0.5$ and $\mathfrak{s}_1/\mathfrak{s}_3 = 0.75$. then take $\beta = 0.5$ for the first case (I) and $\beta = 1.5$ for the second case (II). Note $\beta = 0.5$ corresponds to an intermediate regime between the standard 2D Euler dynamics ($\beta = 0$) and the SQG/3D QG dynamics ($\beta = 1$), while $\beta = 1.5$ corresponds to a regime beyond SQG/3D QG. In general, the flow characteristics vary continuously with β. The values of κ_3 and $\mathfrak{s}_2$ resulting in a finite-time collapse are given in Table 2 along with the collapse time τ.

We use these values as the initial conditions in numerical simulations to determine the trajectories of the point vortices. Eqs. (10) are integrated in time using the standard fourth-order Runge–Kutta scheme with an adaptive time step Δt, controlled by the maximum vortex velocity u_{max}, specifically $\Delta t\, u_{max}(t) = 10^{-4}\, u_{max}(0)$. Following Reinaud [24] we introduce the geometric functions

$$g_i(t) = 1 - \left(\frac{s_i(t)}{\mathfrak{s}_i}\right)^{\beta+2}, \quad i = 1, 2, 3. \tag{28}$$

As follows from (16), if the collapse is exactly self-similar, then $g_1(t) = g_2(t) = g_3(t) = t/\tau$, for $t < \tau$.

Results are presented in Fig. 1 for case I and in Fig. 2 for case II. They show the expected behaviour, validating the equations used to obtain the initial conditions. In both cases, the trajectories of the vortices are spirals and evidently converge to a single point. The evolution of the distances $s_i(t)$ confirms the collapse of the vortex triad at the predicted collapse time $t = \tau$ in Eq. (17) and listed in Table 2. The results also confirm that three distance ratios $s_1(t)/s_2(t)$, $s_3(t)/s_2(t)$ and $s_1(t)/s_3(t)$ are time independent, indicating that the evolution of the vortex triad is self-similar. Moreover, as predicted, the geometrical functions $g_i(t)$ all fall onto the same straight line t/τ.

Table 2 indicates that the values of κ_3 and $\mathfrak{s}_2$ are similar for both cases. The tangential velocity induced by each point vortex falls off as $1/d^{\beta+1}$, where d is the distance from the vortex. Hence, when the vortices are sufficiently close together, the velocity of the point vortices increases as β is increased. This explains why the collapse occurs earlier for $\beta = 1.5$ than it does for $\beta = 0.5$.

We next provide an overview of the conditions which lead to vortex collapse for $\beta = 0.25$, 0.5, 0.75 and 1.5. (The case $\beta = 1$, which models both SQG dynamics ($n = 2$, $\alpha = 1/2$), and 3D QG dynamics ($n = 3$, $\alpha = 1$), is discussed in [24].) Recall that $0 < \beta < n$, with $\beta \to 0$ as $\alpha \to n/2$, and $\beta \to n$ as $\alpha \to 0$. For each value of β, we determine $\mathfrak{s}_2$ and κ_3 in the $(\kappa_2, \mathfrak{s}_1)$ parameter plane. We use 500 values for κ_2 and for $\mathfrak{s}_1$, both equally spaced

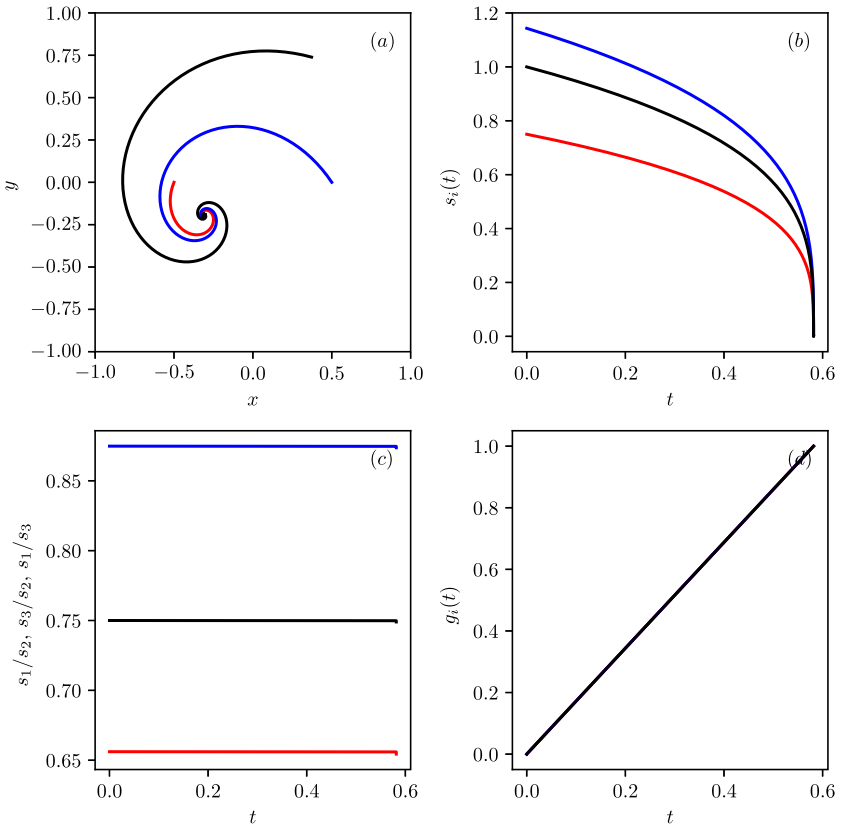

Fig. 2. Evolution of the three point vortices for $\beta = 1.5$, $\kappa_2 = 0.5$ and $\mathfrak{s}_1 = 0.75$ over the interval $0 \le t \le 0.5816$: (a) trajectories of the point vortices, with vortex 1 in red, vortex 2 in blue and vortex 3 in black, (b) distances $s_i(t)$ between the vortices, (c) distance ratios, (d) geometrical functions $g_i(t)$. For panels (b) & (d), $i = 1$ is in red, $i = 2$ is in blue and $i = 3$ is in black. In panel (c), s_1/s_2 is in red, s_3/s_2 is in blue and s_1/s_3 is in black.

in the interval (0, 1]. Results are shown in Fig. 3 (recall we have taken $\mathfrak{s}_3 = 1$, so all distances are effectively scaled by $\mathfrak{s}_3$.)

For a given value of β, and for each value of κ_2, there is a threshold $\mathfrak{s}_1 = S_c$ below which no physical solution exists — collapse cannot occur. The threshold corresponds to $\mathfrak{s}_1^2 - (0.5 - x_3(0))^2 = 0$, i.e. $y_3(0) = 0$ with the three vortices aligned ($\Delta = 0$) and in mutual equilibrium, $\tau \to \infty$. For smaller $\mathfrak{s}_1$ the solution for $y_3(0)$ is purely imaginary and thus not physical. The threshold S_c increases as κ_2 increases. Moreover, for fixed κ_2, the threshold S_c increases as β increases. This means that the range of $\mathfrak{s}_1$ where collapse is possible decreases as both κ_2 and β increase. The left panels of Fig. 3 show that $\mathfrak{s}_2$ remains between 1 and 1.5 throughout parameter space, generally increasing with κ_2 and decreasing with $\mathfrak{s}_1$. The middle panels indicate that κ_3 is only weakly dependent on $\mathfrak{s}_1$, and roughly proportional to κ_2. The right panels show that the collapse time τ reaches a local minimum (along the red dotted line indicated), but over most of the parameter space τ increases with $\mathfrak{s}_1$ and decreases with κ_2. Comparing the different values of β (recall β increases downward), τ generally decreases as β increases. This is consistent with the fact that increasing β means stronger short-range interactions.

The upshot is that, for all κ_2, we can always find vortex triad configurations which collapse self-similarly in finite time. The size of the region of the parameter space where collapse is possible decreases as β increases and as κ_2 increases.

It is worth remarking that β can be larger than 2 if $n > 2$. We have also computed the conditions for collapse when $2 < \beta < 3$. The results exhibit the same trends discussed for $\beta \le 2$ (not shown).

5. Collapse interactions of finite-area vortices, $n = 2$

We next consider the motion of three 2D finite-area vortices, $n = 2$. The initial locations $\boldsymbol{x}_i$ and the rescaled strengths κ_i are chosen to coincide with those of equivalent point vortices collapsing in finite time. Since the far-field flow induced by a finite-area vortex is close to that of an equivalent strength point vortex, the evolution of three well-separated finite-area vortices will closely resemble that of the equivalent point vortex system, provided vortex separations remain large compared with the vortex radii. As vortex separations approach the order of the vortex radii, however, deformations develop on the shape of the vortices. In particular, as two like-signed vortices approach one another a critical separation exists, below which the deformations become large enough that an irreversible (partial) merging of the two like-signed vortices takes place. Since the inward spiralling motion of the vortices collapses their separation, and to the extent that the finite-area vortices follow the point vortex evolution for separations larger than the critical merger distance, we can be confident that vortex merger will always occur for initial conditions coinciding with collapsing point vortices.

We consider vortices with an initially parabolic distribution of the active scalar,

$$q_i(\boldsymbol{x}) = \begin{cases} q_m^i \sqrt{1 - (r'/r_i)^2}, & r' \le r_i, \\ 0, & r > r_j. \end{cases} \tag{29}$$

where q_m^i is the maximum value of the active scalar in the ith vortex, r_i is its radius and $r' = |\boldsymbol{x} - \boldsymbol{x}_i|$ is the radial distance, in $\mathbb{R}^2$, from its centre. In SQG ($n = 2$, $\alpha = 0.5$), this distribution corresponds to a solid-body rotation for $r' < r_i$ for a single

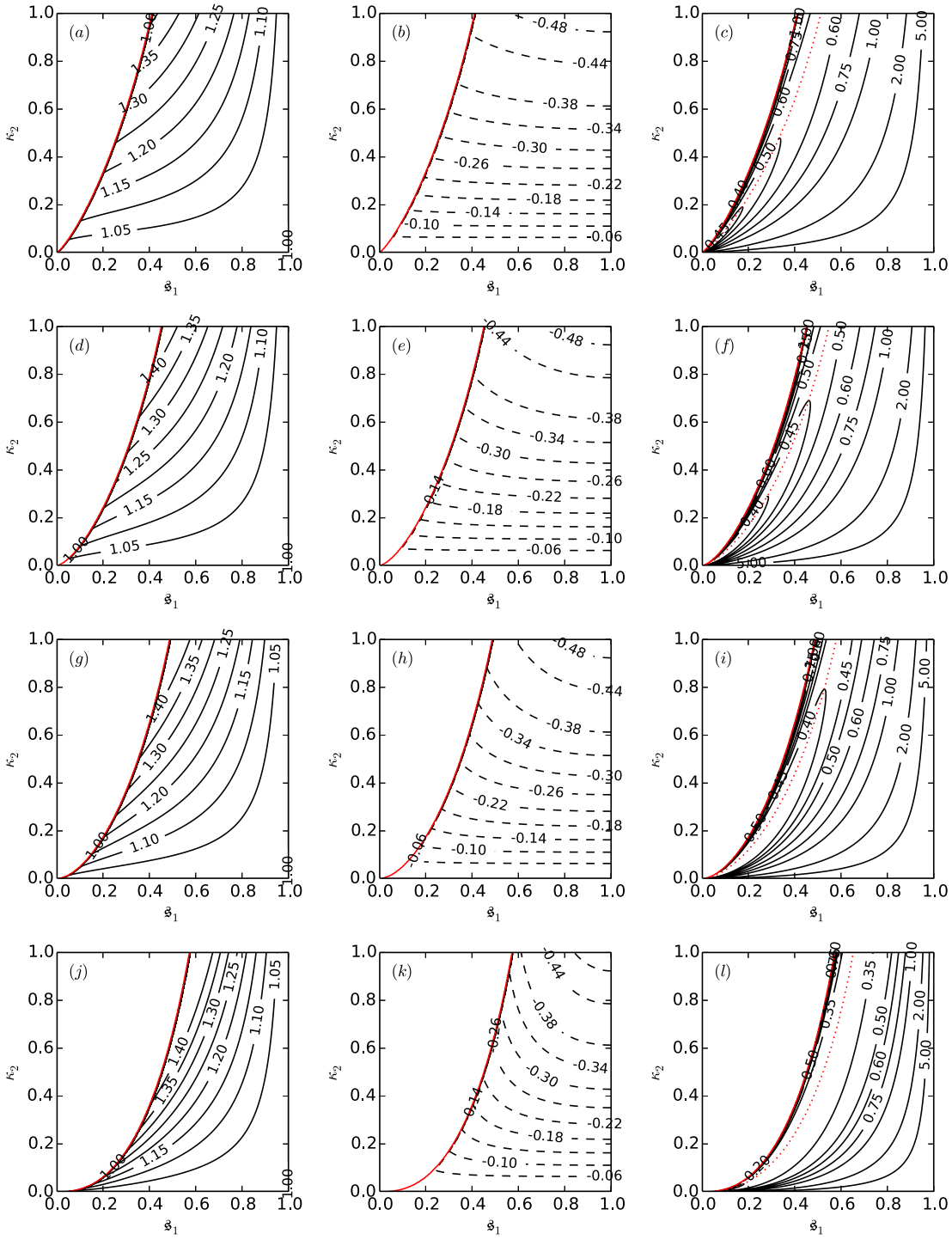

Fig. 3. Conditions for the collapse of three point vortices in the $(\kappa_2, \mathfrak{s}_1)$ parameter plane, with $0 \le \kappa_2, \mathfrak{s}_1 \le 1$. Each row is for fixed β, with $\beta = 0.25$, 0.5, 0.75 and 1.5 from top to bottom. The first column gives the distance $\mathfrak{s}_2$, the second column gives the rescaled vortex strength κ_3, and the third column gives the collapse time τ. The red solid line shows the limit of the parameter space where collapse is possible. Local minima in τ are indicated by the dotted lines in the panels in the right column.

elliptical vortex, see [28] and avoids a logarithmic singularity in tangential velocity that exists in the simpler uniform-patch distribution.

By considering finite-area vortices, we introduce a length scale to the problem: the vortex size. In the examples considered in this section we set $r_1/\mathfrak{s}_3 = 0.2$, unless stated otherwise. The smaller this ratio, the closer the initial system resembles the equivalent point vortex system, and the longer we expect the finite-area vortex evolution to follow the point vortex evolution. Similarly to the point vortices, vortex 1 is initially located at $(x_1, y_1) = (-0.5, 0)$ and vortex 2 at $(x_2, y_2) = (0.5, 0)$, giving $\mathfrak{s}_3 = \ell_{12} = |\boldsymbol{x}_1 - \boldsymbol{x}_2| = 1$. We next set values for the three parameters β, κ_2 and $\mathfrak{s}_1$, then determine κ_3 and $\mathfrak{s}_2$ satisfying the collapse conditions for equivalent point vortices. This allows us to determine the location $\boldsymbol{x}_3$ of the centre of vortex 3. To fully determine vortices 2 and 3, we also need to set q_m^i and r_i, $i = 2, 3$ in order to recover the targeted rescaled strengths κ_2 and κ_3, respectively. There are infinitely many choices. Here we set $|q_m^i| = 1$, $i = 1, 2, 3$.

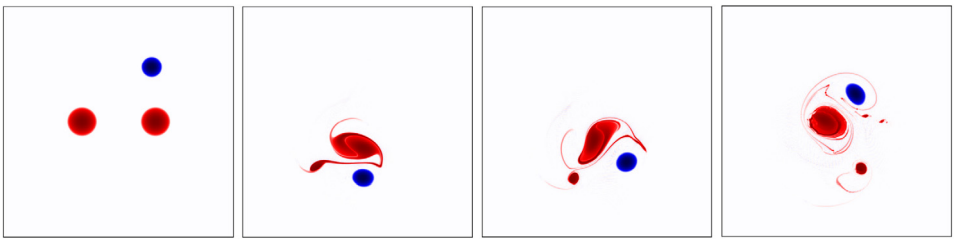

Fig. 4. Top view of the field q showing the collapse of three finite-area vortices in two dimensions, with $\beta = 0.2$ ($\alpha = 0.9$) $\kappa_2/\kappa_1 = 1$ and $\mathfrak{s}_1 = 0.75$, $t = 0$, 70, 77.25 and 100. Only the domain $[-\pi/2, \pi/2]^2$ is shown in the computational domain $[-\pi, \pi]^2$. Positive q is shown in red, negative q is shown in blue. Dark colours correspond to relatively large $|q|$.

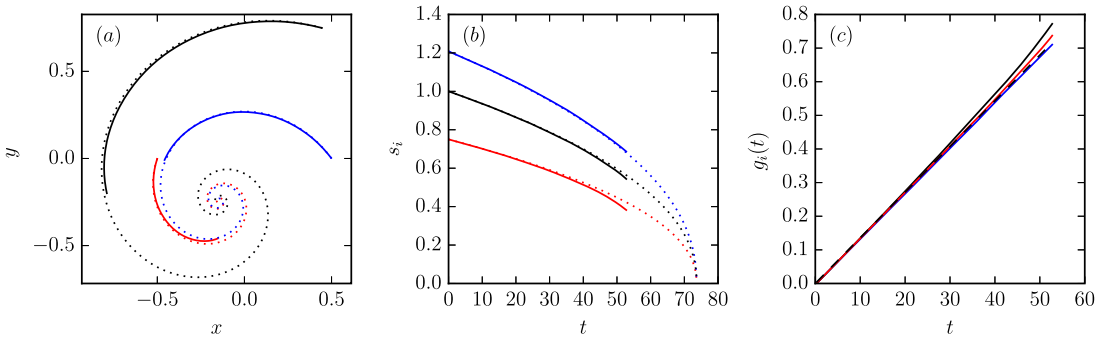

Fig. 5. (a) Trajectories of the three finite-core vortex centres until the like-signed vortices merge (solid lines) and full trajectories for the equivalent point vortices (dotted lines), with vortex 1 in red, vortex 2 in blue and vortex 3 in black, (b) evolution of the distances $s_i(t)$, (c) geometrical functions $g_i(t)$ for $\beta = 0.2$ ($n = 2$, $\alpha = 0.1$) $\kappa_2/\kappa_1 = 1$ and $\mathfrak{s}_1 = 0.75$ (until the two like-signed vortices merge). The dashed black line in (c) shows t/τ_{pv}. In (b) and (c), $i = 1$ is represented in red, $i = 2$ in blue and $i = 3$ in black.

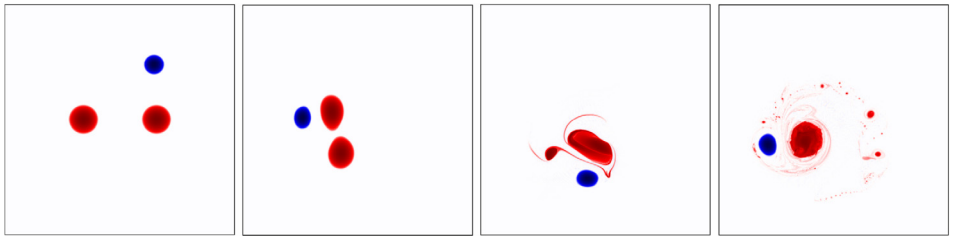

Fig. 6. As in Fig. 4 but for the case $\beta = 0.5$ ($\alpha = 0.75$); the other parameters $\kappa_2/\kappa_1 = 1$ and $\mathfrak{s}_1 = 0.75$ are identical. The times shown are $t = 0$, 39.75, 43, and 100.

Noting that the surface-integrated active scalar for vortex i is $2q_m^i \pi r_i^2/3$, we obtain $\kappa_i = 2\beta C_{2,-\alpha} q_m^i \pi r_i^2/3$. This implies that $|\kappa_i/\kappa_1| = (r_i/r_1)^2$, and we set r_i such that $r_i = r_1\sqrt{|\kappa_i/\kappa_1|}$. Because the focus in this and the following section is on the triggering of vortex merger during the collapse, we present cases mostly of configurations with $\kappa_1 = \kappa_2$; it is in such cases that vortex merger tends to be most efficient and complete.

The equations are solved using the Combined-Lagrangian Advection Method (CLAM), developed by [29], using its standard settings. The fluid domain is $[-\pi, \pi]^2$ and doubly-periodic. The velocity field resolution is 1024^2, while the active scalar is actually resolved down to a scale 16 times finer. In CLAM, Eq. (1) is inverted in spectral space (making use of FFTs).

As a diagnostic, we track the location of the vortex centres. Vortices are identified on the 1024^2 grid as contiguous regions S of active scalar whose value exceeds the root mean square (rms) of the field over the full periodic domain. Their centres (x_q, y_q) are defined as the active scalar-weighted centres of these regions, i.e.

$$(x_q, y_q) = \frac{\iint_S (x, y)\, q\, dA}{\iint_S q\, dA}. \tag{30}$$

It should be noted that the vortices are well confined near the centre of the domain at all times, thus limiting the influence of the periodic images. Because the area-average vorticity is zero, the influence of the periodic images falls off at least as fast as the dipole contribution in the far-field moment expansion.

Fig. 4 shows snapshots of the evolution of the vortex triad for $\beta = 0.2$ ($n = 2$, $\alpha = 0.9$), $\kappa_2/\kappa_1 = 1$ and $\mathfrak{s}_1 = 0.75$. In this case $\kappa_1 \simeq 1.3635 \times 10^{-2}$ and the collapse time of equivalent point vortices is $\tau_{pv} = 73.64$. Fig. 5 shows the trajectories of the vortex centres, the evolution of the distances $s_i(t)$ and the geometrical functions $g_i(t)$ until the two like-signed vortices merge. The merger time t_m is simply detected as the first time when the diagnostic tool identifying the vortices present in the flow only finds two vortices, one being the merged vortex resulting from the fusion of the two like-signed vortices. In this case $t_m = 53$. The left panel of the figure also includes the full trajectories, until $t \to \tau$, of the equivalent point vortices for direct comparison. For $t < t_m$, we see that the vortices start to spiral inwards and closely approach. The match between the trajectories of the finite-area vortex centres and the trajectories of the equivalent point vortices is remarkable. The motion of the vortex centres is very nearly self-similar, as shown in Fig. 5. In particular, the geometrical functions $g_i(t)$ almost fall onto a single straight line which closely agrees with the point vortex prediction, t/τ_{pv}. This is remarkable considering that, near the merger event, the two like-signed vortices have become strongly deformed. The evolution of the vortices shown in Fig. 4 shows the

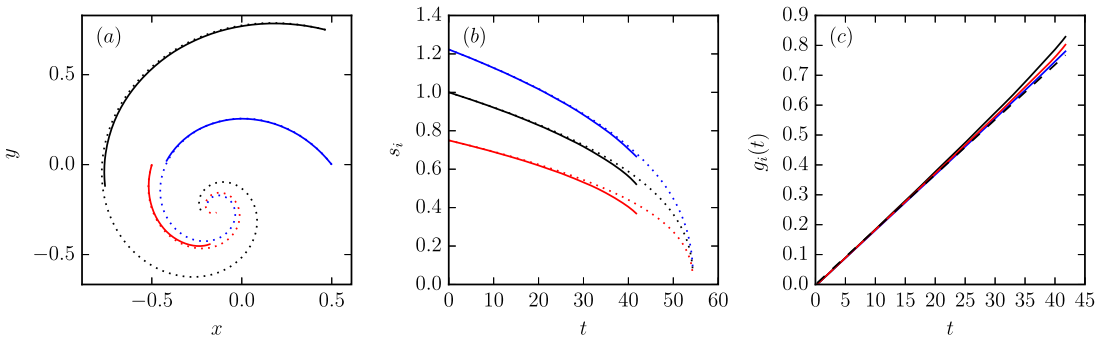

Fig. 7. (*a*) Trajectories of the three finite-core vortex centres until the like-signed vortices merge (solid lines) and full trajectories for the equivalent point vortices (dotted lines), with vortex 1 in red, vortex 2 in blue and vortex 3 in black, (*b*) evolution of the distances $s_i(t)$, (*c*) geometrical functions $g_i(t)$ for $\beta = 0.5$ ($n = 2$, $\alpha = 0.75$), $\kappa_2/\kappa_1 = 1$ and $\mathfrak{s}_1 = 0.75$ (until the two like-signed vortices merge). The dashed black line in (*c*) shows t/τ_{pv}. In (*b*) and (*c*), $i = 1$ is represented in red, $i = 2$ in blue and $i = 3$ in black.

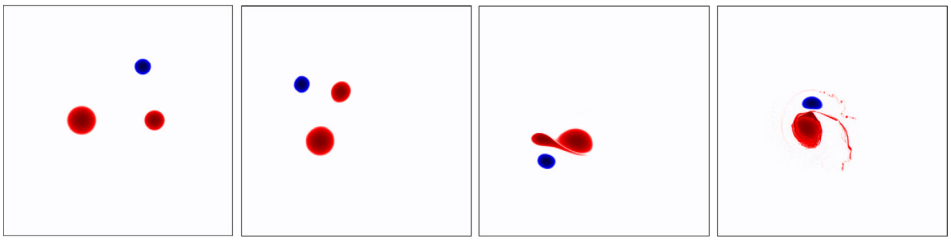

Fig. 8. As in Fig. 6 but for $\kappa_2/\kappa_1 = 0.5$; the other parameters $\beta = 0.5$ ($\alpha = 0.75$) and $\mathfrak{s}_1 = 0.75$ are identical. The times shown are $t = 0$, 49.75, 70, 77.25 and 100.

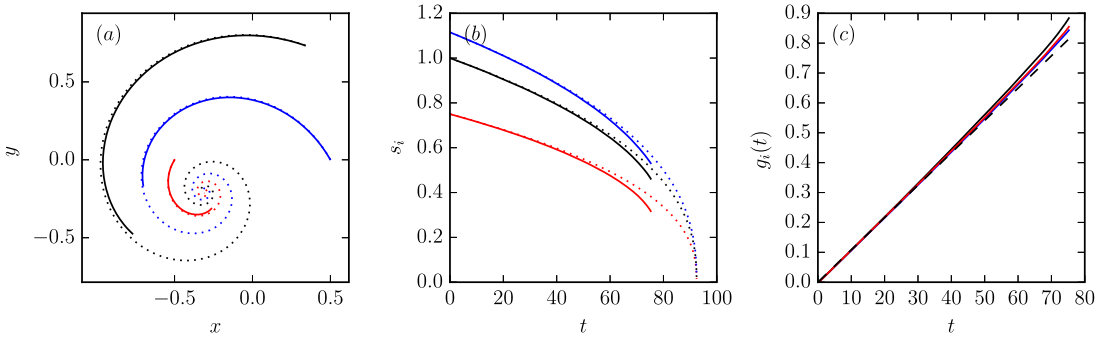

Fig. 9. (*a*) Trajectories of the three finite-core vortex centres until the like-signed vortices merge (solid lines) and full trajectories for the equivalent point vortices (dotted lines), with vortex 1 in red, vortex 2 in blue and vortex 3 in black, (*b*) evolution of the distances $s_i(t)$, (*c*) geometrical functions $g_i(t)$ for $\beta = 0.5$ ($n = 2$, $\alpha = 0.75$), $\kappa_2/\kappa_1 = 0.5$ and $\mathfrak{s}_1 = 0.75$ (until the two like-signed vortices merge). The dashed black line in (*c*) shows t/τ_{pv}. In (*b*) and (*c*), $i = 1$ is represented in red, $i = 2$ in blue and $i = 3$ in black.

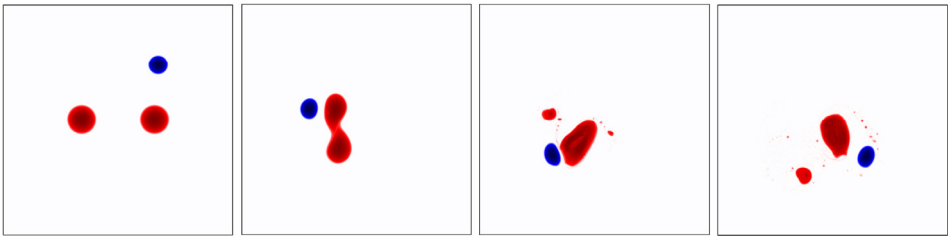

Fig. 10. As in Fig. 4 but for the case $\beta = 1.5$ ($\alpha = 0.25$); the other parameters $\kappa_2/\kappa_1 = 1$ and $\mathfrak{s}_1 = 0.75$ are identical. The times shown are $t = 0$, 31, 33.5 and 44.25.

formation of long filaments that partially wrap around the large coherent vortices. The tail of the largest filament is expelled from the main dipole and experiences a weaker shear than the rest of the filament. It is therefore less stretched and rolls-up as a small secondary positive vortex.

In the next examples we examine the effect of increasing β. Fig. 6 shows snapshots of the evolution of the vortex triad for $\beta = 0.5$ ($n = 2$, $\alpha = 0.75$), with otherwise identical parameters to those considered previously ($\kappa_2 = \kappa_1$ and $\mathfrak{s}_1 = 0.75$). In this case $\kappa_1 \simeq 1.3947 \times 10^{-2}$ and the collapse time of equivalent point vortices is $\tau_{pv} \simeq 54.4$. Fig. 9 shows the trajectories of the vortex centres, the evolution of the distances $s_i(t)$ and the geometrical functions $g_i(t)$ until the two like-signed vortices merge at $t_m = 42$.

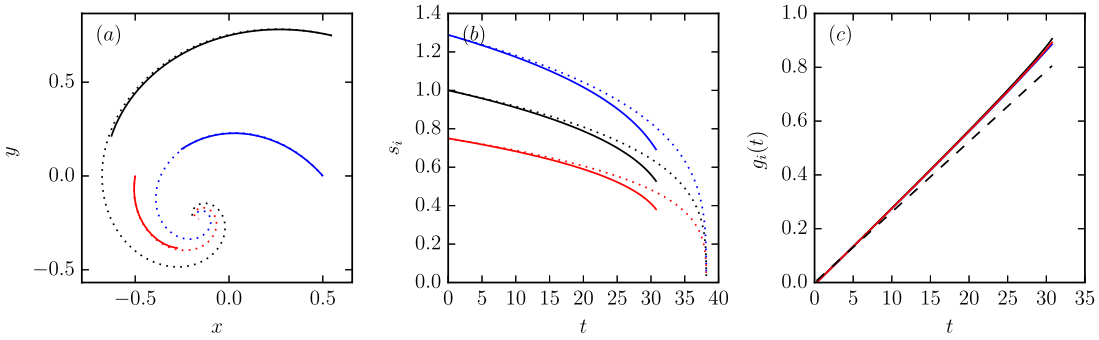

Fig. 11. (*a*) Trajectories of the three finite-core vortex centres until the like-signed vortices merge (solid lines) and full trajectories for the equivalent point vortices (dotted lines), with vortex 1 in red, vortex 2 in blue and vortex 3 in black, (*b*) evolution of the distances $s_i(t)$, (*c*) geometrical functions $g_i(t)$ for $\beta = 1.5$ ($n = 2$, $\alpha = 0.25$), $\kappa_2/\kappa_1 = 1$ and $\mathfrak{s}_1 = 0.75$ (until the two like-signed vortices merge). The dashed black line in (*c*) shows t/τ_{pv}. In (*b*) and (*c*), $i = 1$ is represented in red, $i = 2$ in blue and $i = 3$ in black.

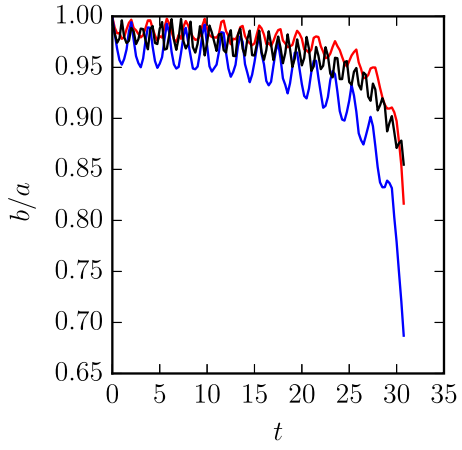

Fig. 12. Evolution of the aspect ratio b/a of the best-fit ellipses for the three vortices for the case $\beta = 1.5$ ($n = 2$, $\alpha = 0.25$), $\kappa_2/\kappa_1 = 1$ and $\mathfrak{s}_1 = 0.75$ (until the two like-signed vortices merge). The red line corresponds to vortex 1, the blue line to vortex 2 and the black line to vortex 3.

As before, the early evolution of the finite-area vortices is remarkably close to that of equivalent point vortices, and the vortices spiral inwardly in a nearly self-similar manner, as shown in panel (*c*) of Fig. 7. Similarly, the three geometrical functions $g_i(t)$, $i = 1, 2, 3$ nearly fall onto the straight line t/τ_{pv} of the exact self-similar point vortex collapse. Again, large filaments of positive q form and are stretched by the differential rotation induced by the large vortex dipole formed after the merger of the two like-signed vortices. We see that the filament is more sensitive however to perturbations in this case, and Kelvin–Helmholtz like roll-ups form along the filament. This is a consequence of the increase in β. The increased sensitivity of filaments has been observed previously when comparing the stability properties of sheared and stretched vortex strips in the standard 2D Euler equations ($\beta = 0$) and in the SQG system ($\beta = 1$), see [30]. This sensitivity is due to shorter-range interactions occurring with increasing β. Both the stabilising effects of adverse shear and stretching [31,32] are reduced, leading to an increased propensity for vortex roll-up.

It is also instructive to consider a case with $\kappa_2 \neq 1$. To this end, Fig. 8 shows snapshots of the evolution of the vortex triad for $\beta = 0.5$ ($n = 2$, $\alpha = 0.75$), $\kappa_2 = 0.5\kappa_1$ and $\mathfrak{s}_1 = 0.75$. As in the previous case, $\kappa_1 \simeq 1.3947 \times 10^{-2}$ but the collapse time of equivalent point vortices is delayed to $\tau_{pv} = 92.42$. Fig. 9 shows the trajectories of the vortex centres, the evolution of the distances $s_i(t)$ and the geometrical functions $g_i(t)$ until the two like-signed vortices merge at $t_m = 75.5$. Then, most of the smaller (weaker) vortex is absorbed by the larger (stronger) one while shedding some of its material into a stretched filament which breaks into smaller vortices. As in the two previous cases, the three geometrical functions $g_i(t)$, $i = 1, 2, 3$ nearly fall onto the straight line t/τ_{pv} of the exact self-similar point vortex collapse.

We next revert back to $\kappa_2/\kappa_1 = 1$ and increase β further. Fig. 10 shows snapshots of the evolution of the vortex triad for $\beta = 1.5$ ($n = 2$, $\alpha = 0.25$), $\kappa_2/\kappa_1 = 1$ and $\mathfrak{s}_1 = 0.75$. In this case $\kappa_1 \simeq 9.5598 \times 10^{-3}$ and $\tau = 38.18$. Fig. 11 shows the trajectories of the vortex centres, the evolution of the distances $s_i(t)$ and the geometrical functions $g_i(t)$ until the two like-signed vortices merge at $t_m = 31$.

Initially, the evolution of the $g_i(t)$ closely follows the straight line t/τ_{pv} before slowly departing from it. Typically $g_i(t) > t/\tau$, indicating that the bigger departures of $s_i(t)$ seen in panel (*b*) of Fig. 11 are due to a time-scale mismatch arising from the deformation of the vortices. The three curves $g_i(t)$, $i = 1, 2, 3$ remain however very close together. It is nonetheless remarkable how closely the trajectories of the finite-area vortex centres and of the point vortices match, indicating that the difference between the two cases is related to a time-scale mismatch. The thin filaments generated during the strong interactions between the vortices rapidly destabilise and break into series of small-scale roll-ups.

We also measure the leading-order deformation of the vortices by determining the aspect ratio b/a, $b \leq a$, of the ellipses best-fit to the vortices. The best-fit ellipse is the ellipse having the same geometrical centre

$$(x_g, y_g) = \frac{\iint_S (x, y)\, dA}{\iint_S dA}, \tag{31}$$

and the same geometrical second order moments M_{xx}, M_{xy} and M_{yy},

$$M_{xx} = \iint_S (x - x_g)^2 dA, \quad M_{xy} = \iint_S (x - x_g)(y - y_g) dA, \quad M_{yy} = \iint_S (y - y_g)^2 dA, \tag{32}$$

as the vortex. Results are shown in Fig. 12. The rapid oscillations of the aspect ratio show that the vortices pulsate. This is a consequence of initially circular vortices rapidly adjusting in the deformation field induced by the other vortices, and then freely pulsating. Note that the pulsation has no discernible impact on the vortex trajectories at any stage of the evolution. Near the merger time the deformation rapidly increases, in particular for vortex 2 which is, at the onset of merger, approximately located between vortices 1 and 3.

To further investigate the small departure of the functions $g_i(t)$ from the analytical prediction of the point vortex triad in this

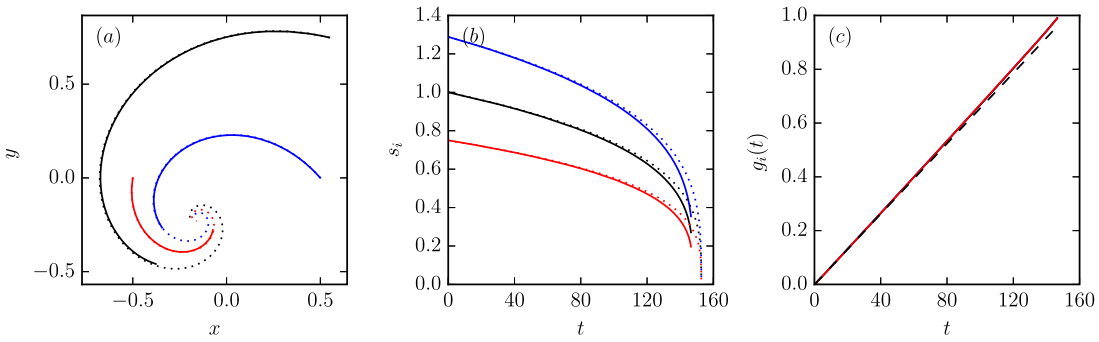

Fig. 13. Same as Fig. 11 but for smaller vortices, with $r_1/\mathfrak{s}_3 = 0.1$.

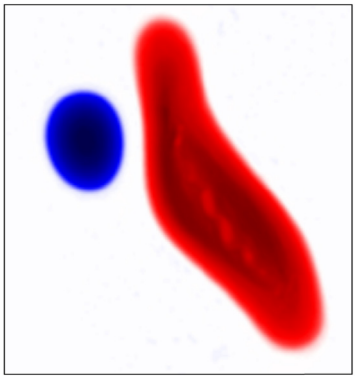

Fig. 14. Close up showing the destabilisation of the shear zone formed between the two like-signed vortices when they merge for $\beta = 1.8$ ($\alpha = 0.1$) $\kappa_2/\kappa_1 = 1$ at $t = 54.4$.

case, we repeat the simulation with smaller, more compact vortices. For a given distance between the vortices, smaller vortices with the same q_m are less sensitive to deformation. We set the radii of all vortices to be half of their previous values by taking $r_1/\mathfrak{s}_3 = 0.1$. Consequently, κ_1, proportional to r_1^2, is 2.3899×10^{-3} or four times smaller, and $\tau_{pv} = 152.7$ is four times larger. The trajectories of the vortex centres, the distances $s_i(t)$ between the vortices, and the geometric functions $g_i(t)$ are presented in Fig. 13. Since the vortices are smaller, they travel further along the spiral trajectories before the two like-signed vortices merge. In this case, the two like-signed vortices merge by $t = 146.75$. The closer agreement with the point vortex trajectories seen here confirms that the small departure observed for $r_1/\mathfrak{s}_3 = 0.2$ is due to finite-core effects, i.e. vortex deformation.

The same general trends are observed if we further increase β. An additional numerical simulation, performed for a vortex triad with $\beta = 1.8$ ($n = 2$, $\alpha = 0.1$), $\kappa_2 = \kappa_1$ and $\mathfrak{s}_1 = 0.75$, exhibits a new route for the generation of small scales when β is large. In this case $r_1/\mathfrak{s}_3 = 0.2$, $\kappa_1 \simeq 4.4694 \times 10^{-3}$, and $\tau_{pv} = 65.49$. As before, the trajectories closely approximate those of the equivalent point vortices at early times, but spiral inward more rapidly at later times (not shown).

The novel feature in this case is shown in Fig. 14, presenting a close up of the vortex interaction at $t = 54.4$. As the two like-signed vortices merge, a strong shear zone develops between them. This shear zone then breaks up into a series of small roll-ups which develop inside the merging structure, leading to a rapid generation of small scales in the flow. This typically happens at larger values of β, when interactions are short range.

6. Collapse interaction of finite-volume vortices, $n = 3$

We next focus on the evolution of finite-volume 3D vortices, $n = 3$. We consider spheres of *uniform* q. Vortex i is thus initially specified by

$$q_i(\boldsymbol{x}) = \begin{cases} q_m^i, & r' < r_i, \\ 0, & r' > r_i \end{cases} \tag{33}$$

where $r' = |\boldsymbol{x} - \boldsymbol{x}_i|$ is the radial distance, in $\mathbb{R}^3$, from the centre of vortex i. In QG ($n = 3$, $\beta = 1$), this corresponds to solid-body rotation for $r < r_i$ for an isolated vortex. It is noteworthy that the uniform distribution (33) is related to the active scalar distribution (29) used in the previous section for $n = 2$, if we flatten the sphere to a disk, but assign the active scalar in the disk half the vertical integral of q over the sphere [28].

To enable collapse, the centres of all three vortices are taken to lie in the plane $z = 0$. As before, vortex 1 is centred at $(-0.5, 0, 0)$ and vortex 2 is centred at $(0, 5, 0, 0)$ such that $\mathfrak{s}_3 = 1$. Inside all three vortices, q takes the same magnitude, $|q_m^i| = 2\pi$. The scaled vortex strength is $\kappa_i = 4C_{3,-\alpha}\beta q_m^i \pi r_i^3/3$, where $C_{n,-\alpha}$ is the constant defined by Eq. (6). We set $r_1/\mathfrak{s}_3 = 0.2$ so that the vortices behave point-like at least for the early stages of the evolution. Since $|\kappa_i/\kappa_1| = (r_i/r_1)^3$, setting a value for κ_2 determines the radius r_2 of vortex 2. Then, setting values for $\mathfrak{s}_1$ and β allows one to determine the location and the radius of vortex 3, using the conditions (25) and (24) for the collapse of point vortices of the same scaled strengths.

The flow evolution is simulated using the Contour-Advective Semi-Lagrangian (CASL) algorithm, introduced in [33] and first adapted to 3D QG dynamics in [34]. As for $n = 2$, Eq. (1) is inverted in spectral space. The flow domain is a triply-periodic cube, with side length 2π.

Vortices are identified as contiguous volumes of uniform q. Their centres are again the active-scalar weighted centres of the vortex volumes, which now coincide with their geometrical centres.

The first example illustrated is for $\beta = 0.5$ ($n = 3$, $\alpha = 1.25$), $\kappa_2 = \kappa_1 \simeq 1.33687 \times 10^{-2}$ and $\mathfrak{s}_1 = 0.75$. The collapse time for equivalent point vortices is $\tau_{pv} = 56.76$. Fig. 15 shows snapshots of the flow and Fig. 16 shows the trajectories of the vortex centres, the evolution of the distances $s_i(t)$ and of the geometrical functions $g_i(t)$ until the vortices merge. The two like-signed vortices merge at $t_m = 52$. By this time, the vortices have already strongly deformed and have departed from the trajectories of the equivalent point vortices. This explains why in this case merger occurs at a later time than the actual collapse time ($\tau_{pv} = 56.76$) of the equivalent point vortices. The early evolution of the vortices does however conform to the self-similar motion of the equivalent point vortices, as shown by the near matching of the geometrical functions $g_i(t)$ with the straight line t/τ_{pv} at early times. Again, large filaments are produced during the strong

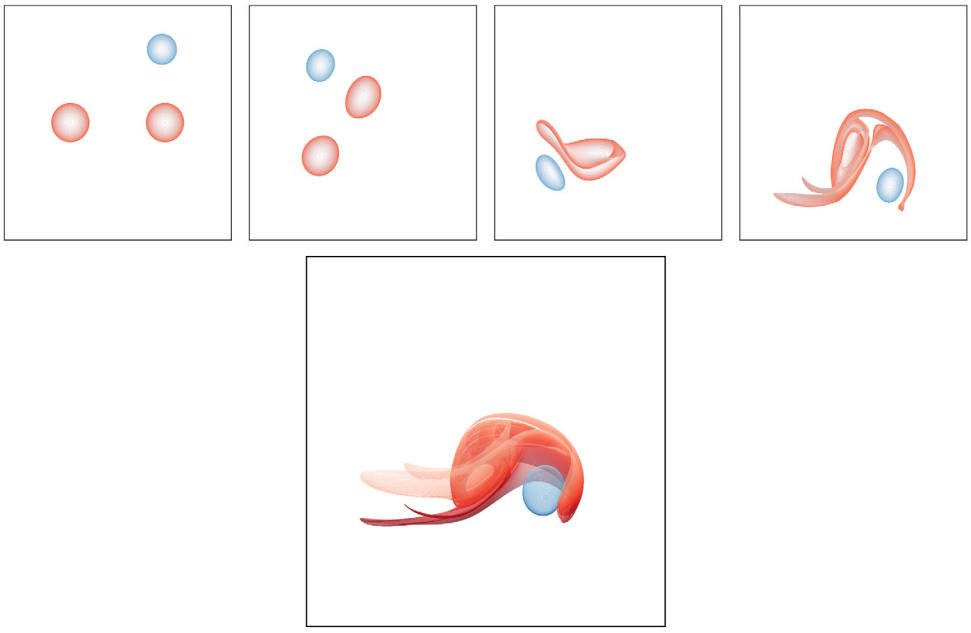

Fig. 15. Top view of the vortex bounding contours in the collapse of three vortices in 3D, for $\beta = 0.5$ ($\alpha = 0.75$), $\kappa_2/\kappa_1 = 1$ and $\mathfrak{s}_1 = 0.75$. Times shown (top row) are $t = 0$, 15, 26 and 35. Orthographic view (bottom row) at an angle of 60° from the vertical at $t = 35$ (bottom row). The shade of the contours indicates the depth: dark contours are near the bottom, while light contours are near the top of the vortices.

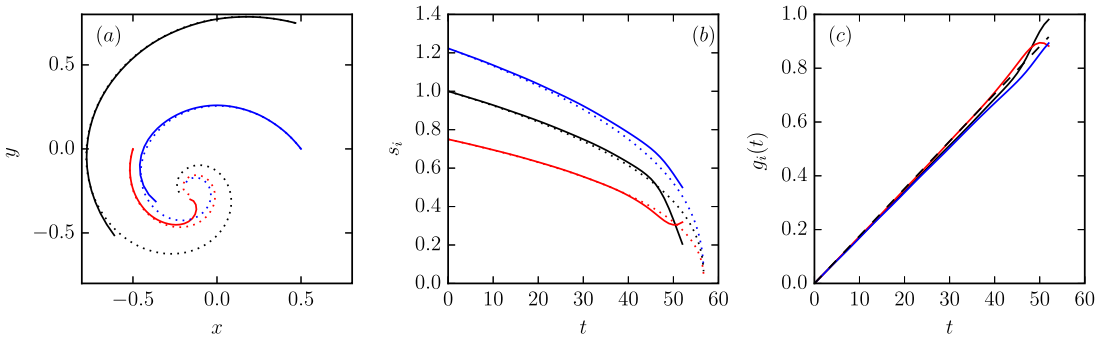

Fig. 16. (a) Trajectories of the three finite-core vortex centres until the like-signed vortices merge (solid lines) and full trajectories for the equivalent point vortices (dotted lines), with vortex 1 in red, vortex 2 in blue and vortex 3 in black, (b) evolution of the distances $s_i(t)$, (c) geometrical functions $g_i(t)$ for $\beta = 0.5$ ($n = 3$, $\alpha = 0.75$) $\kappa_2/\kappa_1 = 1$ and $\mathfrak{s}_1 = 0.75$ (until the two like-signed vortices merge). The dashed black line in (c) shows t/τ_{pv}. In (b) and (c), $i = 1$ is represented in blue, $i = 2$ in red and $i = 3$ in black.

interaction. Filamentation occurs at nearly all heights occupied by the vortices. This produces a highly-convoluted distribution of active scalar.

The last example illustrated is for $\beta = 1.5$ ($n = 3$, $\alpha = 0.25$), $\kappa_2 = \kappa_1 \simeq 2 \times 10^{-2}$ and $\mathfrak{s}_1 = 0.75$. The collapse time for equivalent point vortices is $\tau_{pv} = 18.2$. The two like-signed finite-volume vortices merge at $t_m = 16$. Fig. 17 shows snapshots of the vortices while Fig. 18 shows the trajectories of the vortex centres, the evolution of the distances $s_i(t)$ and of the geometrical functions $g_i(t)$. Results show a very good match between the motion of the vortex centres and the motion of the equivalent point vortices until the like-signed vortices merge, see in particular panel (c) of Fig. 18. Fig. 17 again shows that, during the initial stage of the merger, the vortices are less deformed in this case for $\beta = 1.5$ than in the previous case for $\beta = 0.5$ (having otherwise identical parameters). For $n = 3$ (i.e. 3D), the deformation of the vortices does not affect the geometrical functions $g_i(t)$ as much as it does for $n = 2$ (i.e. 2D). For $\beta = 1.5$, the filaments generated by the interaction are thinner compared to the ones occurring for $\beta = 0.5$, and they break rapidly into small-scale structures. This generates more small-scale secondary coherent vortices and debris. Similarly to the 2D cases, we estimate the vortex deformation by evaluating the aspect ratios b/a and c/a, $c < b < a$, of the best-fit ellipsoids. The best-fit ellipsoid is the ellipsoid having the same geometrical centre and second order moments as the vortex.

Results are shown in Fig. 19. As in the 2D cases, the vortices pulsate weakly. (It should be noted that in this case, by symmetry, the vertical axis of the vortices does not tilt. The intermediate semi-axis length b of the initially spherical vortices, remains constant and corresponds to the vortex half-height. This is a direct consequence of the lack of vertical advection of the vortices. The horizontal aspect ratio is therefore a/c.) Again, at the onset of merger the most deformed vortex is vortex 2.

To quantify the effect of deformation on the vortex trajectories, we measure the difference $|\boldsymbol{\Delta s}(t)|$ between the finite core and equivalent point vortex centres by

$$|\boldsymbol{\Delta s}(t)| = \left(\sum_{i=1}^{3} (s_i(t) - l_i(t))^2 \right)^{1/2} \tag{34}$$

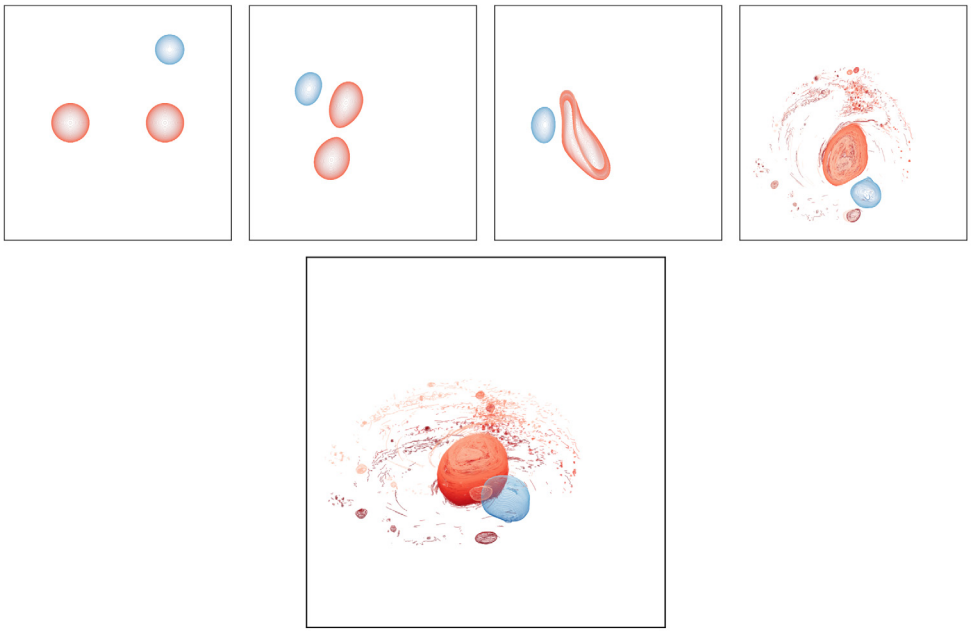

Fig. 17. As in Fig. 15 but for $\beta = 1.5$ ($\alpha = 0.25$); all other parameters are the same, namely $\kappa_2/\kappa_1 = 1$ and $\mathfrak{s}_1 = 0.75$. Times shown (top row) are $t = 0$, 15, 26 and 35. The bottom row again provides an orthographic view of the interaction at $t = 35$.

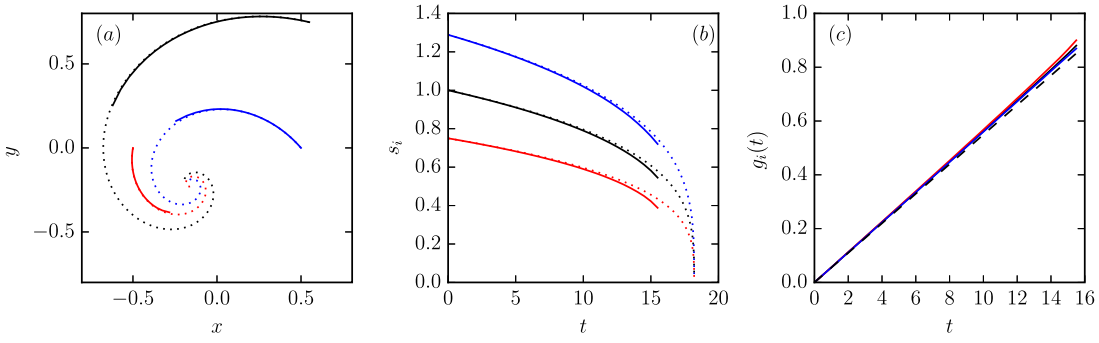

Fig. 18. (a) Trajectories of the three finite-core vortex centres until the like-signed vortices merge (solid lines) and full trajectories for the equivalent point vortices (dotted lines), with vortex 1 in red, vortex 2 in blue and vortex 3 in black, (b) evolution of the distances $s_i(t)$, (c) geometrical functions $g_i(t)$ for $\beta = 1.5$ ($n = 3$, $\alpha = 0.25$), $\kappa_2/\kappa_1 = 1$ and $\mathfrak{s}_1 = 0.75$ (until the two like-signed vortices merge). The dashed black line in (c) shows t/τ_{pv}. In (b) and (c), $i = 1$ is represented in blue, $i = 2$ in red and $i = 3$ in black.

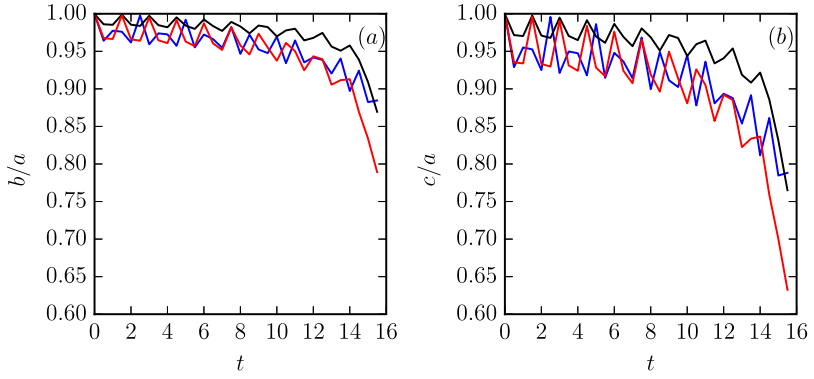

Fig. 19. Evolution of aspect ratios b/a, panel (a), and c/b, panel (b), of the best-fit ellipsoid for the case $\beta = 1.5$ ($n = 3$, $\alpha = 0.25$), $\kappa_2 = \kappa_1 \simeq 2 \times 10^{-2}$ and $\mathfrak{s}_1 = 0.75$ (until the two like-signed vortices merge). The black line corresponds to vortex 1, the red line to vortex 2, the blue line to vortex 3. The jaggedness of the curve is due to the coarse time sampling.

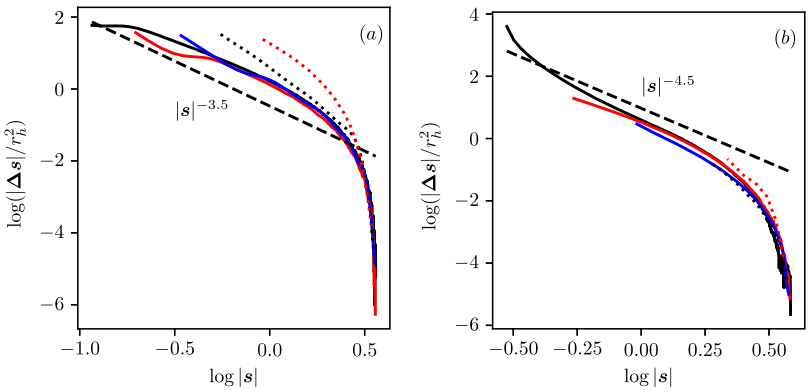

Fig. 20. Scaled difference $|\Delta \boldsymbol{s}(t)|/r_h^2$ (see text for definition) between the finite core and equivalent point vortex trajectories plotted against a measure of the separation of the finite core vortices $|\boldsymbol{s}|$ for (a) $\beta = 0.5$ and (b) $\beta = 1.5$. All simulations are for otherwise identical parameters: $n = 3$, $\kappa_2 = \kappa_1$ and $s_1 = 0.75$. Results are shown for $r_h = 0.1$ (black solid line), 0.15 (red solid line), 0.2 (blue solid line), 0.25 (black dotted line) and 0.3 (red dotted line). Indicative slopes are indicated by black dashed lines: $|\boldsymbol{s}|^{-2.5}$ in (*a*) and $|\boldsymbol{s}|^{-3.5}$ in (*b*).

where s_i and l_i are, respectively, the distances between the finite core vortex centres and between the point vortex centres. We also examine $|\boldsymbol{s}(t)|$, a measure of the distance between the finite core vortex centres, defined similarly (using s_i in place of $s_i - l_i$ on the r.h.s. above). As the vortices spiral toward each other, $|\boldsymbol{s}(t)|$ decreases while $|\Delta \boldsymbol{s}(t)|$ is expected to increase due to the increasing deformation of the vortex cores.

To check this, we have performed additional simulations varying the common radius r_h of the initial vortices while keeping all other parameters fixed. Varying r_h affects the vortex volumes hence their strengths κ_i. In order to compare the results, therefore, we define an equivalent time T

$$T = \left(\frac{r_h}{0.2}\right)^3 t \tag{35}$$

so that $T = t$ for the reference case $r_h = 0.2$. Results are presented in Fig. 20. Here we show $|\Delta \boldsymbol{s}|/r_h^2$ vs $|\boldsymbol{s}|$ before the vortices merge for (a) $\beta = 0.5$ and (b) $\beta = 1.5$, both for $n = 3$, $\kappa_2 = \kappa_1$ and $s_1 = 0.75$. Each curve corresponds to a different radius r_h as indicated. The black dashed lines in these panels give an indicative slope in the middle range of $|\boldsymbol{s}|$ or T (since $|\boldsymbol{s}| \propto (T_c - T)^{1/(\beta+2)}$ for the point vortices). The collapse of the curves indicates that the difference in the finite-core and point-vortex trajectories scales like r_h^2. On the other hand, the dependence on $|\boldsymbol{s}|$ is not a simple power law; there is a much steeper dependence for large $|\boldsymbol{s}|$ than for intermediate values. We cannot provide a theory for this behaviour, but a cursory examination indicates that it is likely to involve a complicated analysis.

7. Conclusion

We have revisited the problem of the finite-time collapse of three vortices in the generalised 2D Euler and 3D QG flow models. For point vortices, the evolution in the two models is identical and only depends on the parameter $\beta = n - 2\alpha$, where n is the dimension of space and α is the power of the Laplacian in the inversion relation between the streamfunction and the active scalar.

We have derived the relations that determine the conditions for finite-time, self-similar collapse from first principles. We then used these conditions to initialise numerical simulations for finite-core vortices in both the 2D and 3D models.

Instead of complete collapse of all three vortices to a point, the interaction leads to the merger of the two like-signed vortices at a time earlier than the point vortex collapse time. We observe both the creation of large scales through vortex merger, and the creation of smaller scales through filamentation and the generation of small-scale debris. These physical processes have been associated with both an inverse energy cascade as well as a direct enstrophy (or active scalar variance) cascade in the past, see e.g. [35]. Indeed, they are likely to be the primary processes for energy and enstrophy transfers in any destructive vortex interaction, not just in turbulent flows. As $\beta = n - 2\alpha$ increases, shear induced by the vortices falls off more rapidly, as $1/d^{\beta+2}$ where d is the distance from the vortex. During strong vortex interactions, the size of the filaments decreases as β increases, and the filaments break down into small-scale structure more rapidly. This offers a rapid route for the generation of small scales in these flows.

The agreement between the finite-core and point vortex evolutions down to vortex separations approaching the critical merger distance, in both the $n = 2$ (2D) and $n = 3$ (3D) cases, is remarkable. As the critical merger distance is approached, vortex deformations inevitably lead to departures from the point vortex trajectories. At that point, qualitative differences in the finite-core deformations between the $n = 2$ and $n = 3$ cases become more pronounced.

In 3D, there is much more freedom for these deformations, and they vary with height. The upper and lower extremities of the vortices are generally more weakly interacting than their midplanes, and are further apart. This has no analogue in 2D, where interactions are on-average at closer range even with the same β. This results in a closer match to the point-vortex dynamics in 3D than in 2D.

The collapse of three vortices is a special case of the more general collapse of N vortices which has been addressed in the literature for 2D flows governed by the standard Euler equations [36] and references therein. The study of the collapse of more than three vortices in generalised Euler and QG flow models is a potential extension of the present work.

CRediT authorship contribution statement

Jean N. Reinaud: Conception and design, Analysis and interpretation of the data, Writing – original draft, Writing – review & editing. **David G. Dritschel:** Conception and design, Analysis and interpretation of the data, Writing – original draft, Writing – review & editing. **Richard K. Scott:** Conception and design, Analysis and interpretation of the data, Writing – original draft, Writing – review & editing.

Declaration of competing interest

The authors declare that they have no known competing financial interests or personal relationships that could have appeared to influence the work reported in this paper.

Acknowledgement

All authors approved the version of the manuscript to be published.

References

[1] J.C. McWilliams, The vortices of two-dimensinal turbulence, J. Fluid Mech. 219 (1990) 361–385.
[2] D.G. Dritschel, R.K. Scott, C. Macaskill, G.A. Gottwald, C.V. Tran, Unifying scaling theory for vortex dynamics in two-dimensional turbulence, Phys. Rev. Lett. 101 (2008) 094501.
[3] B.H. Burgess, R.K. Scott, Scaling theory for vortices in the two-dimensional inverse energy cascade, J. Fluid Mech. 811 (2017) 742–756.
[4] Z. Zhang, W. Wang, B. Qiu, Oceanic mass transport by mesoscale eddies, Science 345 (2014) 322–324.
[5] A. Adriani, A. Mura, G. Orton, C. Hansen, F. Altieri, M.L. Moriconi, J. Rogers, G. Eichtäst, T. Momary, A.P. Ingersoll, G. Filacchione, G. Sindoni, F. Tabataba-Vakili, B.M. Dinelli, F. Fabiano, S.J. Bolton, J.E.P. Connerney, S.K. Atreya, J.I. Lunine, F. Tosi, A. Migliorini, D. Grassi, G. Piccioni, R. Noschese, A. Cicchetti, C. Plainaki, A. Olivieri, M.E. O'Neill, D. Turrini, S. Stefani, R. Sordini, M. Amoroso, Clusters of cyclones encircling Jupiter's poles, Nature 555 (2018) 216–219.
[6] H. von Helmholtz, Über Integrale der hydrodynamischen Gleichungen, welche der Wirbelbewegung entsprechen, J. Reine Angew. Math. 55 (1858) 25–55.
[7] G. Kirchhoff, Vorlesungen Über Mathematische Physik - Mechanik, Druck und Verlag con B.G. Teubner, Leipzig, 1876.
[8] H. Poincaré, Théorie des Tourbillons, George Carré, Paris, 1893.
[9] W. Gröbli, Spezielle Probleme Über die Bewegung Geradliniger Paralleler Wirbelfäden, Druck von Zürcher und Furrer, Zürich, 1877.
[10] J.L. Synge, On the motion of three vortices, Canad. J. Math. 1 (3) (1949) 257–270.
[11] E.A. Novikov, Dynamics and statistics of a system of vortices, Sov. Phys. JETP 41 (1975) 937–943.
[12] H. Aref, Motion of three vortices, Phys. Fluids 22 (1979) 393–400.
[13] J. Tavantzis, L. Ting, The dynamics of three vortices revisited, Phys. Fluids 31 (1988) 1392–1409.
[14] E.A. Novikov, Y.B. Sedov, Vortex collapse, Sov. Phys. JETP 50 (1979) 297–301.
[15] Y. Kimura, Similarity solution of two-dimensional point vortices, J. Phys. Soc. Japan 56 (1987) 2024–2030.
[16] Y. Kimura, Parametric motion of complex-time singularity toward real collapse, Physica D 46 (1990) 439–448.
[17] Y. Kimura, Vortex collapse from the viewpoint of complex-time singularity, Physica D 51 (1991) 512–519.
[18] H. Aref, Self-similar motion of three point vortices, Phys. Fluids 22 (2010) 057104, http://dx.doi.org/10.1063/1.3425649.
[19] V.S. Krishnamurthy, M.A. Stremler, Finite-time collapse of three point vortices in the plane, Regul. Chaotic Dyn. 23 (5) (2018) 530–550.
[20] P.W.C. Vosbeek, J.H.G.M. van Geffen, V.V. Meleshko, G. J.F. van Heijst, Collapse interactions of finite-sized two-dimensional vortices, Phys. Fluids 9 (1997) 3315–3322.
[21] G. Badin, A.M. Barry, Collapse of generalized Euler and surface quasigeostrophic point vortices, Phys. Rev. E 98 (2018) 023110.
[22] C.K. Taylor, s.G. Llewellyn Smith, Dynamics and transport properties of three surface quasigeostrophic point vortices, Chaos 26 (2016) 113117.
[23] J.B. Weiss, Point vortex dynamics in three-dimensional ageostrophic balanced flows, J. Fluid Mech. 936 (2022) A19.
[24] J.N. Reinaud, The self-similar collapse of three geophysical vortices, Geophys. Astrophys. Fluid Dyn. 115 (4) (2021) 369–392.
[25] R.T. Pierrehumbert, I.M. Held, K.L. Swanson, Spectra of local and nonlocal two-dimensional turbulence, Chaos Solitons Fractals 4 (1994) 1111–1116.
[26] I.M. Held, R.T. Pierrehumbert, S.T. Garner, K.L. Swanson, Surface quasi-geostrophic dynamics, J. Fluid Mech. 282 (1995) 1–20.
[27] P.R. Stinga, User's guide to the fractional Laplacian and the method of semigroups, in: A. Kochubei, Y. Luchko (Eds.), Partial Differential Equations, Walter De Gruyter GmbH, Berlin/Munich/Boston, 2019, pp. 235–266.
[28] D.G. Dritschel, An exact steadily rotating surface quasi-geostrophic elliptical vortex, Geophys. Astrophys. Fluid Dyn. 105 (4–5) (2011) 368–376.
[29] D.G. Dritschel, J. Fontane, The combined Lagrangian advection method, J. Comput. Phys. 229 (2010) 5408–5417.
[30] B.J. Harvey, M.H.P. Ambaum, Instability of surface-temperature filaments in strain and shear, Q. J. R. Meterol. Soc. 136 (651) (2010) 1506–1513.
[31] D.G. Dritschel, P.H. Haynes, M.N. Juckes, T.G. Shepherd, The stability of a two-dimensional vorticity filament under uniform strain, J. Fluid Mech. 230 (1991) 647–665.
[32] D.W. Waugh, D.G. Dritschel, The stability of filamentary vorticity in two-dimensional geophysical vortex-dynamics models, J. Fluid Mech. 231 (1991) 575–598.
[33] D.G. Dritschel, M.H. Ambaum, A contour-advective semi-Lagrangian numerical algorithm for simulating fins-scale conservative dynamical fields, Q. J. R. Meterol. Soc. (1997) 1097–1130.
[34] D.G. Dritschel, Vortex merger in rotating stratified flows, J. Fluid Mech. 455 (2002) 83–101.
[35] A.H. Nielsen, X. He, J. Juul Rasmussen, T. Bohr, Vortex merging and spectral cascade of two-dimensional flows, Phys. Fluids 8 (9) (1996) 2263–2265.
[36] H. Kudela, Collapse of n point vortices, formation of the vortex sheets and transport of passive markers, Energies 14 (2021) 943.